

1 Mid-latitude plasma bubbles over China and adjacent 2 areas during a magnetic storm on 08 September 2017

Ercha Aa,^{1,3} Wengeng Huang,¹ Siqing Liu,^{1,2} Aaron Ridley,³ Shasha Zou,³

Liqin Shi,^{1,2} Yanhong Chen,¹ Hua Shen,¹ Tianjiao Yuan,¹ Jianyong Li,⁴ and

Tan Wang⁴

Correspondence to: E. Aa (aercha@nssc.ac.cn)

¹National Space Science Center, Chinese
Academy of Sciences, Beijing, China.

²University of Chinese Academy of
Sciences, Beijing, China.

³Department of Climate and Space
Sciences and Engineering, University of
Michigan, Ann Arbor, USA.

⁴National Earthquake Infrastructure
Service, Beijing, China.

This is the author manuscript accepted for publication and has undergone full peer review but has not been through the copyediting, typesetting, pagination and proofreading process, which may lead to differences between this version and the Version of Record. Please cite this article as doi: [10.1002/2017SW001776](https://doi.org/10.1002/2017SW001776)

Abstract. This paper presents observations of post-sunset super plasma bubbles over China and adjacent areas during the second main phase of a storm on 08 Sep 2017. The signatures of the plasma bubbles can be seen or deduced from: 1) deep field-aligned total electron content (TEC) depletions embedded in regional ionospheric maps derived from dense Global Navigation Satellite System (GNSS) networks; 2) significant equatorial and mid-latitude plasma bite-outs in electron density measurements onboard Swarm satellites; 3) enhancements of ionosonde virtual height and scintillation in local evening associated with strong southward interplanetary magnetic field (IMF). The bubbles/depletions covered a broad area mainly within 20° - 45° N and 80° - 110° E with bifurcated structures and persisted for nearly 5 hours (\sim 13-18 UT). One prominent feature is that the bubbles extended remarkably along the magnetic field lines in the form of depleted flux tubes, reaching up to mid-latitude of around 50° N (MLAT: 45.5° N) that maps to an altitude of 6600 km over the magnetic equator. The maximum upward drift speed of the bubbles over the magnetic equator was about 700 m/s, and gradually decreased with altitude and time. The possible triggering mechanism of the plasma bubbles was estimated to be storm-time eastward prompt penetration electric field (PPEF), while the traveling ionospheric disturbance (TID) could play a role in facilitating the latitudinal extension of the depletions.

1. Introduction

24 Plasma bubbles refer to irregular structures of plasma density depletion, which are
25 typical characteristics of nighttime ionosphere over equatorial and low-latitude regions.
26 Plasma bubbles with different scale sizes can manifest themselves as spread-F echoes on
27 ionograms [Abdu *et al.*, 2003], plume-like structures in radar backscatter maps [Woodman
28 and La Hoz, 1976], airglow density depletions in all-sky images [Kelley *et al.*, 2002],
29 and VHF/UHF scintillations of satellites signals [Bhattacharyya *et al.*, 2001; Basu *et al.*,
30 2005]. It is widely considered that the plasma bubbles are generated by the Rayleigh-
31 Taylor (R-T) instability in the bottom-side ionosphere after sunset and evolve nonlinearly
32 penetrating the F peak to the topside ionosphere [Kelley *et al.*, 1976; Ott, 1978; Fejer
33 *et al.*, 1999; Ma and Maruyama, 2006]. They sometimes form into wedge-like structures
34 extended along the magnetic field lines [Tsunoda, 1980; Tsunoda *et al.*, 1982]. Although
35 various mechanisms (such as electric field, neutral wind, and gravity waves) can play a
36 role in triggering R-T instability, the most efficient seeding factor of plasma bubbles over
37 equatorial/low-latitude regions is the zonal electric field [e.g., Abdu *et al.*, 1997; Fejer *et al.*,
38 1999; Li *et al.*, 2009a; Kil, 2015]. The post-sunset enhancement of eastward electric field,
39 also known as pre-reversal enhancement (PRE), is responsible for the enhanced equatorial
40 upward drift that causes density perturbations to grow by the R-T instability mechanism,
41 which may lead to the formation of plasma bubbles [Farley *et al.*, 1986; Retterer and
42 Roddy, 2014; Abdu, 2012; Abadi *et al.*, 2015].

43 During geomagnetic storms, the development of plasma bubbles can be enhanced or sup-
44 pressed depending primarily on two types of perturbation electric fields: (1) the prompt

45 penetration electric field (PPEF) created by solar wind-magnetosphere dynamo associ-
46 ated with southward turning of IMF B_z ; (2) ionospheric disturbance dynamo electric field
47 (DDEF) induced by changes in global thermospheric circulation due to auroral Joule heat-
48 ing, which may lead to the inhibition of post-sunset plasma bubbles occurrence [*Scherliess*
49 *and Fejer*, 1997; *Li et al.*, 2009b; *Ramsingh et al.*, 2015; *Carter et al.*, 2016]. The PPEF
50 can be superposed on the normal dusk PRE to cause larger ionospheric uplift and thus
51 facilitate the development of plasma bubbles [*Abdu et al.*, 2003; *Basu et al.*, 2001, 2007;
52 *Tulasi Ram et al.*, 2008; *Huang et al.*, 2010]. The storm effect of these two competing
53 mechanisms on plasma bubbles is an important concern in ionosphere research community.

54 The occurrence of plasma bubbles and associated signatures of irregularities can even
55 be observed at middle latitude, which could be caused either by an extension of equatorial
56 plasma bubbles along the magnetic field lines after rising to a relatively high altitude, or
57 by local Perkins instability [*Perkins*, 1973]. Recently, several studies have indicated that
58 the equatorial plasma irregularities can reach high altitudes and extend to higher latitudes
59 in the form of depleted flux tubes. For example, it was reported by *Kelley et al.* [2003] and
60 *Makela and Kelley* [2003] that the equatorial plasma depletions can be viewed in all-sky
61 airglow images at Maui, Hawaii (MLAT: 21.3°N). *Mendillo et al.* [2005, 2018] conducted
62 simultaneous observation by using radar measurements and all-sky images at Arecibo
63 observatory (MLAT: 30°N), and the study showed that the field-aligned structures in the
64 images corresponding to the flux tubes of plasma density depletions. *Ma and Maruyama*
65 [2006] reported a case in which a super plasma bubble could be detected at MLAT 31°N
66 by using dense GPS network observations. *Foster and Rich* [1998] reported that the
67 plasma depletions can be measured at MLAT 35°-37°N by using Millstone Hill incoherent

68 scatter radar and the DMSP satellites. *Katamzi-Joseph et al.* [2017] found that the plasma
69 bubbles can extend as far north as $\sim 42^\circ\text{N}$ (MLAT: $\sim 39^\circ\text{N}$) using GNSS TEC and ion
70 measurements from DMSP satellites. *Cherniak and Zakharenkova* [2016] reported super
71 plasma bubbles in Europe for more than 8 h reaching $\sim 40^\circ\text{-}45^\circ\text{N}$ (MLAT: $\sim 35^\circ\text{-}41^\circ\text{N}$),
72 based on GNSS TEC as well as measurements from Swarm and DMSP satellites. *Huang*
73 *et al.* [2007] reported that during intense storms, depleted flux tubes associated with
74 large-scale plasma bubbles can extend to much higher latitudes (MLAT: $\sim 46^\circ\text{N}$).

75 In this paper, we present unique observations of super plasma bubbles at MLAT $\sim 15^\circ\text{-}$
76 45°N over China and adjacent areas during an intense storm on 08 Sep 2017. It was found
77 that the storm-time PPEF contributed to the generation and migration of the super
78 plasma bubbles, which were detected and recorded by using observations from ionosonde,
79 dense GNSS network, and the Swarm satellites. Moreover, TID could also played a role
80 in facilitating the latitudinal extension of the bubbles.

2. Data Description

81 Measurements from multiple instruments were analyzed to study the characteristics of
82 plasma bubbles under the influence of the geomagnetic storm on 08 Sep 2017. The solar
83 wind and geomagnetic conditions during the storm are described in Figure 1 by using solar
84 wind speed, interplanetary magnetic field (IMF) B_z component, interplanetary electric
85 field (IEF) E_y component, the longitudinal asymmetric index (ASY-H) that represents
86 the auroral activity, and the symmetric index (SYM-H) as the high-resolution Dst index.

87 The most important information about plasma bubbles are provided by the TEC data
88 from ground-based GNSS measurements. The GNSS data come from Crustal Movement
89 Observation Network of China (CMONOC) and the International GNSS Service (IGS).

90 CMONOC consists of 260 GNSS receivers covering China mainland, and there are 38
91 stations of IGS located within China and adjacent regions. For more details on the
92 distribution of GNSS stations and the procedures of TEC derivation, readers may refer
93 to *Aa et al.* [2015].

94 Besides TEC data, the ionosonde measurements from Sanya (18.3°N, 109.4°E) and
95 GNSS scintillation measurements from Kunming (24.2°N, 103.4°E) and Guangzhou(23.2°N,
96 113.3°E), as well as the in situ electron density measurements on board the Swarm A and
97 Swarm C satellites at an orbit at altitude around 450 km are used to analyze the signature
98 of plasma bubbles.

3. Observational Results

99 During the time periods of 07-08 Sep 2017, two coronal mass ejections (CME) passed
100 Earth successively and generated an intense geomagnetic storm with a double main phase.
101 Figures 1a-1e show the temporal variation of the solar wind speed, IMF B_z component,
102 IEF E_y component, SYM-H index, and the ASY-H index for the above-mentioned periods.
103 Figures 1a and 1b show that the IMF B_z turned southward at around 20:40 UT on 07
104 Sep and remained negative at nearly constant level for 2 hours, then suddenly decreased
105 to a minimum value of -31.2 nT at 23:31 UT on 07 Sep, along with a sharp increase of
106 the solar wind speed due to the compression and interaction of these two CMEs. Figure
107 1d illustrates that the minimum value of SYM-H for the first storm main phase reached
108 -144 nT at 01:05 UT on 08 Sep. During the recovery phase, the next CME re-amplified
109 the storm with a second main phase onset at 11:35 UT. The IMF B_z decreased to -17.4
110 nT at 11:55 UT on 08 Sep and remained negative for several hours. SYM-H dropped to
111 a second minimum value of -111 nT at 17:05 UT on 08 Sep.

112 Figure 1f shows the corresponding variation of ionospheric virtual height ($h'F$) over a low
113 latitude station Sanya (18.3°N , 109.4°E , dip angle: 11.3°). The local dusk to dawn inter-
114 vals of the station on 08 Sep are marked by shaded areas. Figure 1f shows that compared
115 with the previous evening, the $h'F$ of Sanya station exhibited a considerable post-sunset
116 increase at around 12:45 UT on 08 Sep, which was consistent with the pronounced increase
117 (decrease) of IEF E_y (SYM-H). These near simultaneous enhancements of $h'F$ and IEF E_y
118 indicate that there was a prompt penetration of eastward electric field into middle and low
119 latitude regions at local dusk hours on 08 Sep, which added onto the normal post-sunset
120 PRE of zonal electric field, caused larger upward plasma drifts, and generated conditions
121 favorable for the formation of plasma bubbles. Figures 1g and 1h show the measurements
122 of L-band amplitude scintillations index S4 from GPS/Beidou satellites in the adjacent
123 stations: Kunming (24.2°N , 103.4°E , dip angle: 17.7°) and Guangzhou (23.2°N , 113.3°E ,
124 dip angle: 16.7°). Weak to moderate scintillations started from around 11:45-12:00 UT
125 on 08 Sep, illustrating the possible generation of plasma irregularities/bubbles induced by
126 the geomagnetic storm.

127 TEC data can be used to further confirm the existence of plasma bubbles. Figures
128 2 and 3 show a series of gridded vertical TEC maps over China and adjacent areas at
129 15 min intervals during 12:45-17:00 UT on 08 Sep 2017. An elevation cutoff of 30° was
130 used to avoid multi-paths effects. The resolution of the map is $1^\circ \times 1^\circ$ and was generated
131 by selecting the median of all available measurements in each bin as the estimated grid
132 value, with no interpolation being applied. The signatures of the plasma bubbles appeared
133 in the form of TEC depletions embedded in the maps mainly within 20° - 45°N and 80° -
134 110°E , which originated from the equatorial latitudes and then expanded northwestward

135 approximately along the geomagnetic field lines. The depth of TEC depletions varied
136 in the range of 5-15 TEC Unit (TECU, 10^{16} el/m²). As shown in Figures 2b and 2c,
137 two separate parallel structures of TEC depletion initiated around 13:00 UT, which could
138 correspond to bifurcated branches of plasma bubbles as previously reported [e.g., *Ma and*
139 *Maruyama*, 2006; *Cherniak and Zakharenkova*, 2016].

140 In order to further illustrate the characteristics of plasma bubbles, the rate of TEC
141 index (ROTI) [*Pi et al.*, 1997] was derived by using dual frequency phase measurements of
142 navigation signals, which can be used to represent the severity of GNSS phase fluctuations
143 and to characterize the ionospheric irregularities. The time derivative of TEC (Rate of
144 TEC change, ROT) was first calculated for all visible satellites with elevation angle greater
145 than 30°. ROTI is defined as the 5-min standard deviation of ROT. For more details
146 about ROTI, readers may refer to *Pi et al.* [1997] and *Cherniak et al.* [2014]. Figures
147 4 and 5 present the ROTI maps with the same resolution and time interval as those of
148 Figures 2 and 3. The irregularities were first seen in the low latitude regions between
149 95°E and 120°E longitudinal sectors at 12:45 UT, which approximately corresponded to
150 a local time between 19:00 and 20:45. The bubble-like structures bifurcated and further
151 extended northwestward in the form of depleted flux tubes. The west branch reached
152 $\sim 45^\circ\text{N}$ (MLAT: $\sim 41^\circ\text{N}$) at 13:30 UT, indicating that the plasma bubbles could rise to an
153 altitude of ~ 4800 km over the magnetic equator. Similarly, the east branch migrated to a
154 maximum latitude of $\sim 50^\circ\text{N}$ (MLAT: $\sim 45.5^\circ\text{N}$) that corresponded to an altitude of ~ 6600
155 km over the magnetic equator, similar to those indicated in *Huang et al.* [2007]. TEC
156 depletion and associated ROTI fluctuation continued for 5 hours and gradually subsided.

157 Figures 6a-6g show the temporal variation of ionospheric pierce points (IPP) vertical
158 TEC at seven stations between 10-16 UT on 08 Sep 2017 for PRNs 10, 18, 21, and 24.
159 The locations of these stations are shown in Figure 2i, which were selected to be evenly
160 distributed along the latitudinal extension of the irregularities as much as possible. The
161 color-bar represents the geographic latitudes of IPP, indicating that TEC depletions can
162 be observed between 15°N to 50°N . Figures 6h-6n show the associated de-trended TEC
163 results to better illustrate the plasma depletion. The de-trended TEC was calculated
164 by subtracting the 1-hour moving average value of original TEC data. The inclined red
165 thick line marks the trends of the negative wavefront. This can be used to calculate the
166 horizontal phase speed of the depletion, which is estimated to be as much as ~ 800 m/s
167 with roughly a northwestward direction. Considering the previous analysis of Figures
168 2 and 4, the rate of latitudinal extension of the depletion/irregularities traces in TEC
169 and ROTI maps can be used to estimate the vertical drift speed of equatorial plasma
170 bubbles. The scintillation started at around 1145 UT at Kunming station (MLAT: 17.7°),
171 which corresponded to ~ 650 km altitude over magnetic equator; while the highest latitude
172 reached by the TEC/ROTI at ~ 1315 UT is 45°N (MLAT: 40.5°), which corresponded
173 to ~ 4600 km altitude over magnetic equator. It can be estimated that the upward drift
174 speed of plasma bubbles over the magnetic equator was ~ 700 m/s at around 13:15 UT
175 and gradually decreased with increasing altitude and time.

176 Figure 7 shows satellite passes and the corresponding measurements of electron density
177 from the Swarm constellation from 12 UT to 18 UT on 08 Sep 2017. Swarm A and Swarm
178 C flew at an altitude of 440-460 km. They have nearby longitudes that approximately
179 located in ~ 10 LT (ascending) and ~ 22 LT (descending) sectors. The geographic maps

with different satellite orbit paths between 60°N-60°S are shown in Figures 7a and 7b for Swarm A and C, respectively. The right panels show the variation of in situ electron density (Ne) with respect to latitude along these paths. Swarm B is not shown here since its did not pass over China and adjacent sectors in the local post-sunset hours during this storm period. Swarm A measured no signatures of equatorial plasma bubbles in paths #1 (147°E) and #2 (123°E), though obvious plasma depletions were detected at ~40°S. However, the satellite in path #3 (100°E) measured a wide and drastic density depletion near the equator as low as 2×10^3 el/cm², which was 2-3 orders of magnitude lower than normal Ne conditions. The coverage of major depletion was between 10°S and 20°N with several minor negative spikes distributed in the middle latitudes of both hemispheres, which can be clearly distinguished from the main ionospheric mid-latitude trough at around 50°-60°. Similar observations were made by Swarm C as shown in Figure 7b. The TEC results that coincide with path #3 (#8) at 15:15 UT and with path #4 (#9) at 16:45 UT are also superimposed on Figures 7a and 7b, respectively. Recall from Figures 3b and 3h that the same paths of Swarm were also shown there with four intersections between satellite paths and TEC depletions being marked. It can be seen that these intersections (X1-X4) correspond nicely to the mid-latitude bite-outs in the plasma profiles. This demonstrates that the latitudinal elongated plasma depletion was mainly associated with plasma bubbles, though another factor that the Swarm orbit being below the F layer peak might also play a role in it. This bubble-associated extension of depletion was also reported by several studies [e.g. *Basu et al.*, 2001; *Kil et al.*, 2006; *Huang et al.*, 2007; *Cherniak and Zakharenkova*, 2016]. These studies indicate that the plasma bubbles can be lifted to higher altitudes with depletions being extended along the

203 magnetic field lines to higher latitudes, as can be seen in paths #4 (#9) and #5 (#10).
204 The equatorial Ne depletions along these paths were less obvious and gradually subsided,
205 yet the signatures of plasma bubbles that had drifted to much higher latitudes can be
206 detected at $\sim 50^\circ\text{N}$ and $\sim 40^\circ\text{S}$. The shaded areas indicate deep plasma depletions over
207 China and adjacent regions in accord with TEC depletions in Figures 2 and 3 as well as
208 ROTI fluctuations in Figures 4 and 5.

4. Discussion

209 Firstly, the results presented in the previous section indicate that there were significant
210 equatorial plasma bubbles over China and adjacent sectors in local dusk hours on 08 Sep
211 2017, which were associated with strong PPEF as can be deduced from the simultaneously
212 drastic change of IMF B_z , IEF, SYM-H, and ionosphere virtual height during the second
213 main phase of the storm. It is generally assumed that PPEF is eastward (westward)
214 during daytime through dusk sectors (midnight to dawn sectors), and can penetrate nearly
215 instantly to low latitudes and has a relatively short duration ($\sim 1\text{-}2$ h); On the other hand,
216 DDEF is westward (eastward) during daytime (nighttime), and the build-up time of the
217 DDEF after storm onset is comparatively long (>3 h) such that it may take up to 1-2 days
218 before the equatorial ionospheric response can be fully observed [*Fejer, 1991; Li et al.,*
219 *2009b; Horvath and Lovell, 2013; Tulası Ram et al., 2015*]. *Huang [2008]* and *Huang et al.*
220 *[2010]* also pointed out that the PPEF is approximately proportional to the IEF during
221 the storm main phase. Recall from Figures 1c and 1f that the IEF E_y drastically increased
222 from -6.5 mV/m (11:35 UT) to 13.76 mV/m (11:58 UT) on 08 Sep 2017, and h'F at Sanya
223 station exhibited considerable increase simultaneously. This eastward IEF corresponds to
224 eastward PPEF. In addition, the evolution of TEC depletion and ROTI fluctuation were

225 also consistent with the variation of IMF B_z , IEF E_y , and SYM-H, which collectively
226 show that it was the PPEF that drove the development of equatorial plasma bubbles.

227 Secondly, recent studies have shown that the PPEF can persist with considerably longer
228 durations of ~ 8 -10h if the IMF B_z is sustained southward for prolonged periods [*Huang*
229 *et al.*, 2005; *Huang*, 2008]. Recall from Figure 1b that during the second main phase of
230 the storm on 08 Sep, the IMF B_z suddenly dropped to -17.4 nT at 11:55 UT and remained
231 southward for several hours, which suggests that there was a continuous PPEF since 12:00
232 UT. Moreover, some studies found that the PPEF could be eastward even at 22-23 LT
233 [e.g. *Fejer et al.*, 2008; *Chakrabarty et al.*, 2015], which may be the case for this event that
234 is evidenced in Figure 7, which shows that significant equatorial plasma depletions were
235 measured along path #3 of Swarm A and path #8 of Swarm C at around 15.5 UT (~ 22
236 LT). It appears therefore that a possible extension of the upward vertical drift towards
237 longer duration due to the consistent PPEF might have contributed to the bubble growth
238 rate.

239 Thirdly, one important aspect regarding the plots from Figures 2 to 5 is that the TEC
240 irregularity traces were displaced westward in the successive plots and further the declina-
241 tion of the traces with the N-S meridian increases as time increases. These characteristics
242 suggest that the irregularity structures drift westward with velocity increasing with in-
243 creasing latitude. Since the observation of bubbles was preceded by the first main phase
244 of storm event about 12 hours earlier, there is possibility of atmospheric gravity waves
245 (AGWs) that generated in auroral zone and propagated equatorward, which could create
246 traveling ionospheric disturbance (TID) that acted on the field-aligned bubble traces to
247 shape such a latitude dependent drift.

248 Last but not least, mid-latitude plasma irregularities can either be an extension of
249 depleted plasma bubbles from the equator [e.g., *Ma and Maruyama, 2006; Huang et al.,*
250 *2007; Cherniak and Zakharenkova, 2016; Katamzi-Joseph et al., 2017*], or generated due to
251 the AGWs and/or coupling between Perkins and sporadic E (E_s) layer instabilities, which
252 will manifest in the form of TID [e.g., *Shiokawa et al., 2002, 2003; Tsugawa et al., 2007; Li*
253 *et al., 2009a*]. Considering nighttime medium-scale TID could generate stream-like struc-
254 tures with southwestward propagation direction, it is very likely that both mechanisms
255 played a role in current study. The storm-time PPEF initiated the uplift of equatorial
256 plasma bubbles and generated the latitudinal extension of the plasma depletions; while
257 the TID might further facilitate the stretch of this structure and make it tilt more west-
258 ward. Thus the vertical drift velocity and the highest altitude of the equatorial plasma
259 bubbles that estimated in the previous section are likely to be the upper limit. More work
260 need to be done in the future to distinguish the effects between plasma bubbles and TID.

5. Conclusion

261 This study presented unique observations of super plasma bubbles with bifurcated struc-
262 tures in the evening sector within China and adjacent areas (20° - 45° N and 80° - 110° E)
263 during a storm on 08 Sep 2017. The existence and characteristics of the plasma bubbles
264 were well indicated by the following results: 1) significant GNSS TEC decrease for 5-15
265 TECU and Swarm Ne depletions for 2-3 orders of magnitude; 2) enhancement of iono-
266 spheric h'F and associated equatorial plasma uplifts over certain stations after strongly
267 southward turning of IMF; 3) severe regional irregularities in ROTI map that is aligned
268 with the TEC depletion structure. It has been shown that the plasma bubbles and uplifts
269 were triggered by eastward PPEF. The upward drift speed of equatorial plasma bubbles

270 was as much as 700 m/s at around 13 UT and gradually decreased with altitude and
271 time. This study provides useful evidence in demonstrating the link between equatorial
272 and mid-latitude electrodynamics. The observed plasma depletions persisted for several
273 hours and expanded northwestward along the magnetic field lines to mid-latitude regions,
274 which could be attributed to both equatorial plasma bubbles and medium-scale TID. The
275 highest latitude where the depletions reached was around 50°N (MLAT: 45.5°N), which
276 suggest that the plasma bubbles might reach an apex height of 6600 km over the magnetic
277 equator. However, this estimation is likely to be an upper limit since the transition of
278 depletion signature from one of plasma bubbles to that of TID is not well defined, which
279 need to be studied in the future.

280 **Acknowledgments.** This work is sponsored by the National Key R&D Program of
281 China (2016YFB0501503), National Science Foundation of China (41404125, 41674183),
282 and Youth Innovation Promotion Association of Chinese Academy of Sciences. The
283 CMONOC data are available from the National Earthquake Infrastructure Service of
284 China after registration approval via email at (cmonoc@seis.ac.cn). The IGS data
285 are acquired from NASA Earth Science Data Systems that archived and distributed
286 by the Crustal Dynamics Data Information System (CDDIS). The IMF B_z and IEF
287 E_y data are obtained from the NASA Goddard Space Flight Center Omniweb In-
288 terface (<https://omniweb.gsfc.nasa.gov>). ASY-H and SYM-H indices are obtained
289 from the World Data Center for Geomagnetism, Kyoto University (wdc.kugi.kyoto-
290 u.ac.jp). We greatly appreciate the University of Massachusetts Lowell for provid-
291 ing ionosonde data from the DIDB database of Global Ionospheric Radio Observatory
292 (<http://spase.info/SMWG/Observatory/GIRO>).

References

- 293 Aa, E., W. Huang, S. Liu, L. Shi, J. Gong, Y. Chen, and H. Shen (2015), A regional iono-
294 spheric TEC mapping technique over China and adjacent areas: GNSS data processing
295 and DINEOF analysis, *Sci. China Inf. Sci.*, *58*(10), 1–11, doi:10.1007/s11432-015-5399-
296 2.
- 297 Abadi, P., Y. Otsuka, and T. Tsugawa (2015), Effects of pre-reversal enhancement of $E \times$
298 B drift on the latitudinal extension of plasma bubble in Southeast Asia, *Earth, Planets,*
299 *and Space*, *67*, 74, doi:10.1186/s40623-015-0246-7.
- 300 Abdu, M. A. (2012), Equatorial spread F/plasma bubble irregularities under
301 storm time disturbance electric fields, *J. Atmos. Terr. Phys.*, *75*, 44–56, doi:
302 10.1016/j.jastp.2011.04.024.
- 303 Abdu, M. A., J. H. Sastri, J. MacDougall, I. S. Batista, and J. H. A. Sobral (1997),
304 Equatorial disturbance dynamo electric field longitudinal structure and spread F: A
305 case study from GUAR/EITS Campaigns, *Geophys. Res. Lett.*, *24*, 1707–1710, doi:
306 10.1029/97GL01465.
- 307 Abdu, M. A., I. S. Batista, H. Takahashi, J. MacDougall, J. H. Sobral, A. F. Medeiros,
308 and N. B. Trivedi (2003), Magnetospheric disturbance induced equatorial plasma bubble
309 development and dynamics: A case study in Brazilian sector, *J. Geophys. Res.*, *108*,
310 1449, doi:10.1029/2002JA009721.
- 311 Basu, S., S. Basu, K. M. Groves, H.-C. Yeh, S.-Y. Su, F. J. Rich, P. J. Sultan, and M. J.
312 Keskinen (2001), Response of the equatorial ionosphere in the South Atlantic Region
313 to the Great Magnetic Storm of July 15, 2000, *Geophys. Res. Lett.*, *28*, 3577–3580,
314 doi:10.1029/2001GL013259.

- 315 Basu, S., S. Basu, K. M. Groves, E. MacKenzie, M. J. Keskinen, and F. J. Rich (2005),
316 Near-simultaneous plasma structuring in the midlatitude and equatorial ionosphere dur-
317 ing magnetic superstorms, *Geophys. Res. Lett.*, *32*, L12S05, doi:10.1029/2004GL021678.
- 318 Basu, S., S. Basu, F. J. Rich, K. M. Groves, E. MacKenzie, C. Coker, Y. Sahai, P. R.
319 Fagundes, and F. Becker-Guedes (2007), Response of the equatorial ionosphere at dusk
320 to penetration electric fields during intense magnetic storms, *J. Geophys. Res.*, *112*,
321 A08308, doi:10.1029/2006JA012192.
- 322 Bhattacharyya, A., S. Basu, K. M. Groves, C. E. Valladares, and R. Sheehan (2001),
323 Dynamics of equatorial F region irregularities from spaced receiver scintillation obser-
324 vations, *Geophys. Res. Lett.*, *28*, 119–122, doi:10.1029/2000GL012288.
- 325 Carter, B. A., E. Yizengaw, R. Pradipta, J. M. Retterer, K. Groves, C. Valladares,
326 R. Caton, C. Bridgwood, R. Norman, and K. Zhang (2016), Global equatorial plasma
327 bubble occurrence during the 2015 St. Patrick’s Day storm, *J. Geophys. Res. Space*
328 *Physics*, *121*, 894–905, doi:10.1002/2015JA022194.
- 329 Chakrabarty, D., D. Rout, R. Sekar, R. Narayanan, G. D. Reeves, T. K. Pant, B. Veenad-
330 hari, and K. Shiokawa (2015), Three different types of electric field disturbances affect-
331 ing equatorial ionosphere during a long-duration prompt penetration event, *J. Geophys.*
332 *Res. Space Physics*, *120*, 4993–5008, doi:10.1002/2014JA020759.
- 333 Cherniak, I., and I. Zakharenkova (2016), First observations of super plasma bubbles in
334 Europe, *Geophys. Res. Lett.*, *43*, 11, doi:10.1002/2016GL071421.
- 335 Cherniak, I., A. Krankowski, and I. Zakharenkova (2014), Observation of the ionospheric
336 irregularities over the Northern Hemisphere: Methodology and service, *Radio Sci.*, *49*,
337 653–662, doi:10.1002/2014RS005433.

- 338 Farley, D. T., E. Bonelli, B. G. Fejer, and M. F. Larsen (1986), The prereversal en-
339 hancement of the zonal electric field in the equatorial ionosphere, *J. Geophys. Res.*, *91*,
340 13,723–13,728, doi:10.1029/JA091iA12p13723.
- 341 Fejer, B. G. (1991), Low latitude electrodynamic plasma drifts - A review, *J. Atmos. Terr.*
342 *Phys.*, *53*, 677–693, doi:10.1016/0021-9169(91)90121-M.
- 343 Fejer, B. G., L. Scherliess, and E. R. de Paula (1999), Effects of the vertical plasma drift
344 velocity on the generation and evolution of equatorial spread F, *J. Geophys. Res.*, *104*,
345 19,859–19,870, doi:10.1029/1999JA900271.
- 346 Fejer, B. G., J. W. Jensen, and S.-Y. Su (2008), Seasonal and longitudinal dependence
347 of equatorial disturbance vertical plasma drifts, *Geophys. Res. Lett.*, *35*, L20106, doi:
348 10.1029/2008GL035584.
- 349 Foster, J. C., and F. J. Rich (1998), Prompt midlatitude electric field effects during severe
350 geomagnetic storms, *J. Geophys. Res.*, *103*, 26,367–26,372, doi:10.1029/97JA03057.
- 351 Horvath, I., and B. C. Lovell (2013), Equatorial westward electrojet impacting equatorial
352 ionization anomaly development during the 6 April 2000 superstorm, *J. Geophys. Res.*,
353 *118*, 7398–7409, doi:10.1002/2013JA019311.
- 354 Huang, C.-S. (2008), Continuous penetration of the interplanetary electric field to the
355 equatorial ionosphere over eight hours during intense geomagnetic storms, *J. Geophys.*
356 *Res.*, *113*, A11305, doi:10.1029/2008JA013588.
- 357 Huang, C.-S., J. C. Foster, and M. C. Kelley (2005), Long-duration penetration of the
358 interplanetary electric field to the low-latitude ionosphere during the main phase of
359 magnetic storms, *J. Geophys. Res.*, *110*, A11309, doi:10.1029/2005JA011202.
- 360 Huang, C.-S., J. C. Foster, and Y. Sahai (2007), Significant depletions of the ionospheric

- 361 plasma density at middle latitudes: A possible signature of equatorial spread F bubbles
362 near the plasmopause, *J. Geophys. Res.*, *112*, A05315, doi:10.1029/2007JA012307.
- 363 Huang, C.-S., F. J. Rich, and W. J. Burke (2010), Storm time electric fields in the equa-
364 torial ionosphere observed near the dusk meridian, *J. Geophys. Res.*, *115*, A08313,
365 doi:10.1029/2009JA015150.
- 366 Katamzi-Joseph, Z. T., J. B. Habarulema, and M. Hernández-Pajares (2017), Midlatitude
367 postsunset plasma bubbles observed over europe during intense storms in april 2000 and
368 2001, *Space Weather*, *15*(9), 1177–1190, doi:10.1002/2017SW001674.
- 369 Kelley, M. C., G. Haerendel, H. Kappler, A. Valenzuela, B. B. Balsley, D. A. Carter,
370 W. L. Ecklund, C. W. Carlson, B. Haeusler, and R. Torbert (1976), Evidence for a
371 Rayleigh-Taylor type instability and upwelling of depleted density regions during equa-
372 torial spread F, *Geophys. Res. Lett.*, *3*, 448–450, doi:10.1029/GL003i008p00448.
- 373 Kelley, M. C., J. J. Makela, B. M. Ledvina, and P. M. Kintner (2002), Observations
374 of equatorial spread-F from Haleakala, Hawaii, *Geophys. Res. Lett.*, *29*, 2003, doi:
375 10.1029/2002GL015509.
- 376 Kelley, M. C., J. J. Makela, L. J. Paxton, F. Kamalabadi, J. M. Comberiate, and H. Kil
377 (2003), The first coordinated ground- and space-based optical observations of equatorial
378 plasma bubbles, *Geophys. Res. Lett.*, *30*, 1766, doi:10.1029/2003GL017301.
- 379 Kil, H. (2015), The Morphology of Equatorial Plasma Bubbles - a review, *J. Astron. Space*
380 *Sci.*, *32*, 13–19, doi:10.5140/JASS.2015.32.1.13.
- 381 Kil, H., L. J. Paxton, S.-Y. Su, Y. Zhang, and H. Yeh (2006), Characteristics
382 of the storm-induced big bubbles (SIBBs), *J. Geophys. Res.*, *111*, A10308, doi:
383 10.1029/2006JA011743.

- 384 Li, G., B. Ning, B. Zhao, L. Liu, W. Wan, F. Ding, J. S. Xu, J. Y. Liu, and K. Yumoto
385 (2009a), Characterizing the 10 November 2004 storm-time middle-latitude plasma bub-
386 ble event in Southeast Asia using multi-instrument observations, *J. Geophys. Res.*, *114*,
387 A07304, doi:10.1029/2009JA014057.
- 388 Li, G., B. Ning, L. Liu, W. Wan, and J. Y. Liu (2009b), Effect of magnetic activity on
389 plasma bubbles over equatorial and low-latitude regions in East Asia, *Ann. Geophys.*,
390 *27*, 303–312, doi:10.5194/angeo-27-303-2009.
- 391 Ma, G., and T. Maruyama (2006), A super bubble detected by dense GPS network at
392 east Asian longitudes, *Geophys. Res. Lett.*, *33*, L21103, doi:10.1029/2006GL027512.
- 393 Makela, J. J., and M. C. Kelley (2003), Field-aligned 777.4-nm composite airglow images of
394 equatorial plasma depletions, *Geophys. Res. Lett.*, *30*, 1442, doi:10.1029/2003GL017106.
- 395 Mendillo, M., E. Zesta, S. Shodhan, P. J. Sultan, R. Doe, Y. Sahai, and J. Baumgardner
396 (2005), Observations and modeling of the coupled latitude-altitude patterns of equato-
397 rial plasma depletions, *J. Geophys. Res.*, *110*, A09303, doi:10.1029/2005JA011157.
- 398 Mendillo, M., D. Hickey, C. Martinis, J. Wroten, and J. Baumgardner (2018), Space
399 weather nowcasting for area-denied locations: Testing all-sky imaging applications at ge-
400 omagnetic conjugate points, *Space Weather*, *16*(1), 47–56, doi:10.1002/2017SW001741.
- 401 Ott, E. (1978), Theory of Rayleigh-Taylor bubbles in the equatorial ionosphere, *J. Geo-*
402 *phys. Res.*, *83*, 2066–2070, doi:10.1029/JA083iA05p02066.
- 403 Perkins, F. (1973), Spread F and ionospheric currents, *J. Geophys. Res.*, *78*, 218–226,
404 doi:10.1029/JA078i001p00218.
- 405 Pi, X., A. J. Mannucci, U. J. Lindqwister, and C. M. Ho (1997), Monitoring of global
406 ionospheric irregularities using the Worldwide GPS Network, *Geophys. Res. Lett.*, *24*,

- 407 2283–2286, doi:10.1029/97GL02273.
- 408 Ramsingh, S. Sripathi, S. Sreekumar, S. Banola, K. Emperumal, P. Tiwari, and B. S.
409 Kumar (2015), Low-latitude ionosphere response to super geomagnetic storm of 17/18
410 March 2015: Results from a chain of ground-based observations over Indian sector, *J.*
411 *Geophys. Res. Space Physics*, *120*, 10, doi:10.1002/2015JA021509.
- 412 Retterer, J. M., and P. Roddy (2014), Faith in a seed: on the origins of equatorial plasma
413 bubbles, *Ann. Geophys.*, *32*, 485–498, doi:10.5194/angeo-32-485-2014.
- 414 Scherliess, L., and B. G. Fejer (1997), Storm time dependence of equatorial dis-
415 turbance dynamo zonal electric fields, *J. Geophys. Res.*, *102*, 24,037–24,046, doi:
416 10.1029/97JA02165.
- 417 Shiokawa, K., Y. Otsuka, T. Ogawa, N. Balan, K. Igarashi, A. J. Ridley, D. J. Knipp,
418 A. Saito, and K. Yumoto (2002), A large-scale traveling ionospheric disturbance dur-
419 ing the magnetic storm of 15 September 1999, *J. Geophys. Res.*, *107*, 1088, doi:
420 10.1029/2001JA000245.
- 421 Shiokawa, K., C. Ihara, Y. Otsuka, and T. Ogawa (2003), Statistical study of nighttime
422 medium-scale traveling ionospheric disturbances using midlatitude airglow images, *J.*
423 *Geophys. Res.*, *108*, 1052, doi:10.1029/2002JA009491.
- 424 Tsugawa, T., Y. Otsuka, A. J. Coster, and A. Saito (2007), Medium-scale traveling iono-
425 spheric disturbances detected with dense and wide TEC maps over North America,
426 *Geophys. Res. Lett.*, *34*, L22101, doi:10.1029/2007GL031663.
- 427 Tsunoda, R. T. (1980), Magnetic-field-aligned characteristics of plasma bubbles in the
428 nighttime equatorial ionosphere, *J. Atmos. Terr. Phys.*, *42*, 743–752, doi:10.1016/0021-
429 9169(80)90057-4.

- 430 Tsunoda, R. T., R. C. Livingston, J. P. McClure, and W. B. Hanson (1982), Equatorial
431 plasma bubbles - Vertically elongated wedges from the bottomside F layer, *J. Geophys.*
432 *Res.*, *87*, 9171–9180, doi:10.1029/JA087iA11p09171.
- 433 Tulasi Ram, S., P. V. S. Rama Rao, D. S. V. V. D. Prasad, K. Niranjana, S. Gopi
434 Krishna, R. Sridharan, and S. Ravindran (2008), Local time dependent response
435 of postsunset ESF during geomagnetic storms, *J. Geophys. Res.*, *113*, A07310, doi:
436 10.1029/2007JA012922.
- 437 Tulasi Ram, S., S. Kumar, S.-Y. Su, B. Veenadhari, and S. Ravindran (2015), The influ-
438 ence of Corotating Interaction Region (CIR) driven geomagnetic storms on the devel-
439 opment of equatorial plasma bubbles (EPBs) over wide range of longitudes, *Adv. Space*
440 *Res.*, *55*, 535–544, doi:10.1016/j.asr.2014.10.013.
- 441 Woodman, R. F., and C. La Hoz (1976), Radar observations of F region equatorial irreg-
442 ularities, *J. Geophys. Res.*, *81*(31), 5447–5466, doi:10.1029/JA081i031p05447.

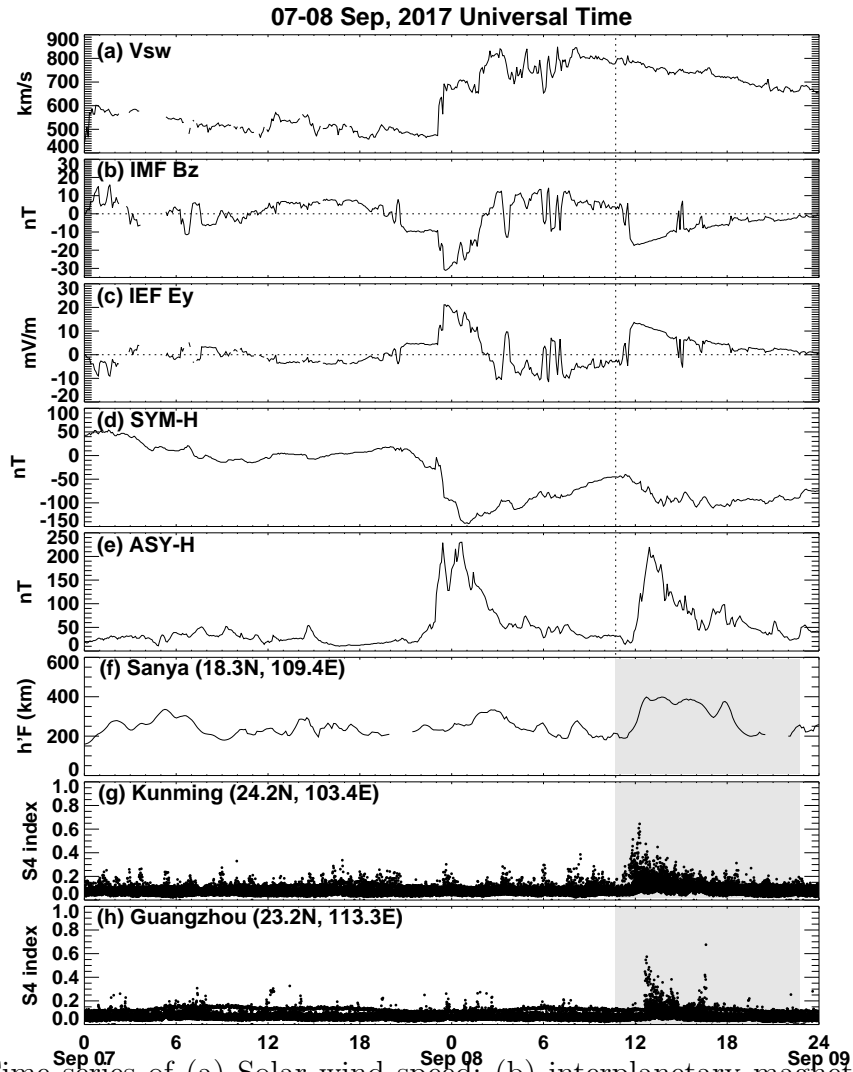


Figure 1. Time series of (a) Solar wind speed; (b) interplanetary magnetic field (IMF) B_z , (c) interplanetary electric field (IEF) E_y , (d) SYM-H index, (e) ASY-H index, (f) ionospheric virtual height ($h'F$) over Sanya, and S4 scintillation index during the period of 07-08 September 2017 for Kunming (g) and Guangzhou (h). The solar wind and IMF data have been shifted to the nose of the Earth's bow shock. The shaded areas represent the local dusk to dawn period at these stations.

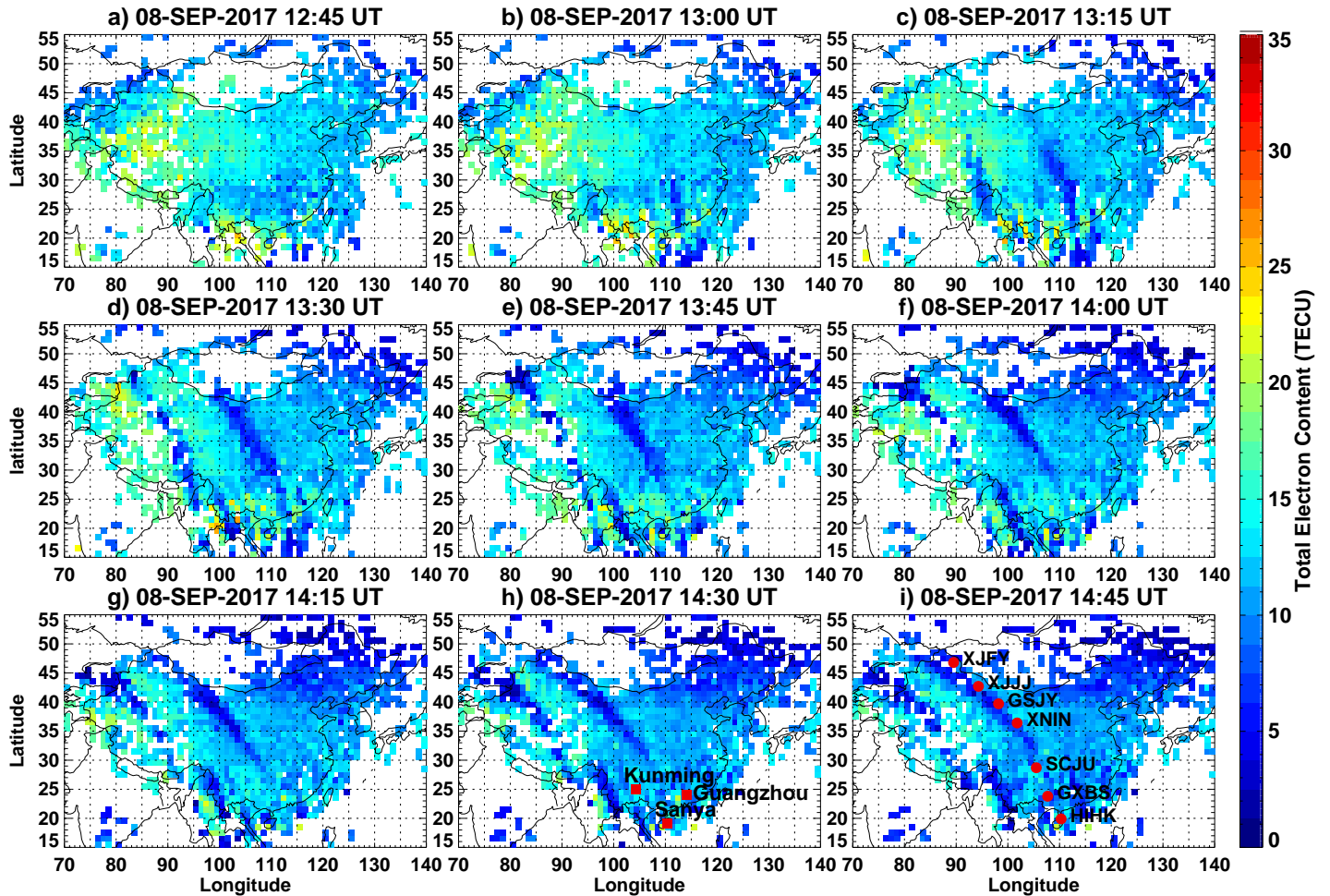


Figure 2. Gridded TEC maps over China and adjacent areas with 15 min interval during 12:45-14:45 UT on 08 September 2017. The distribution of ionosonde/scintillation stations used in current study are shown in Figure 2h. Seven GNSS stations are marked in Figure 2i to track the trace of irregularities.

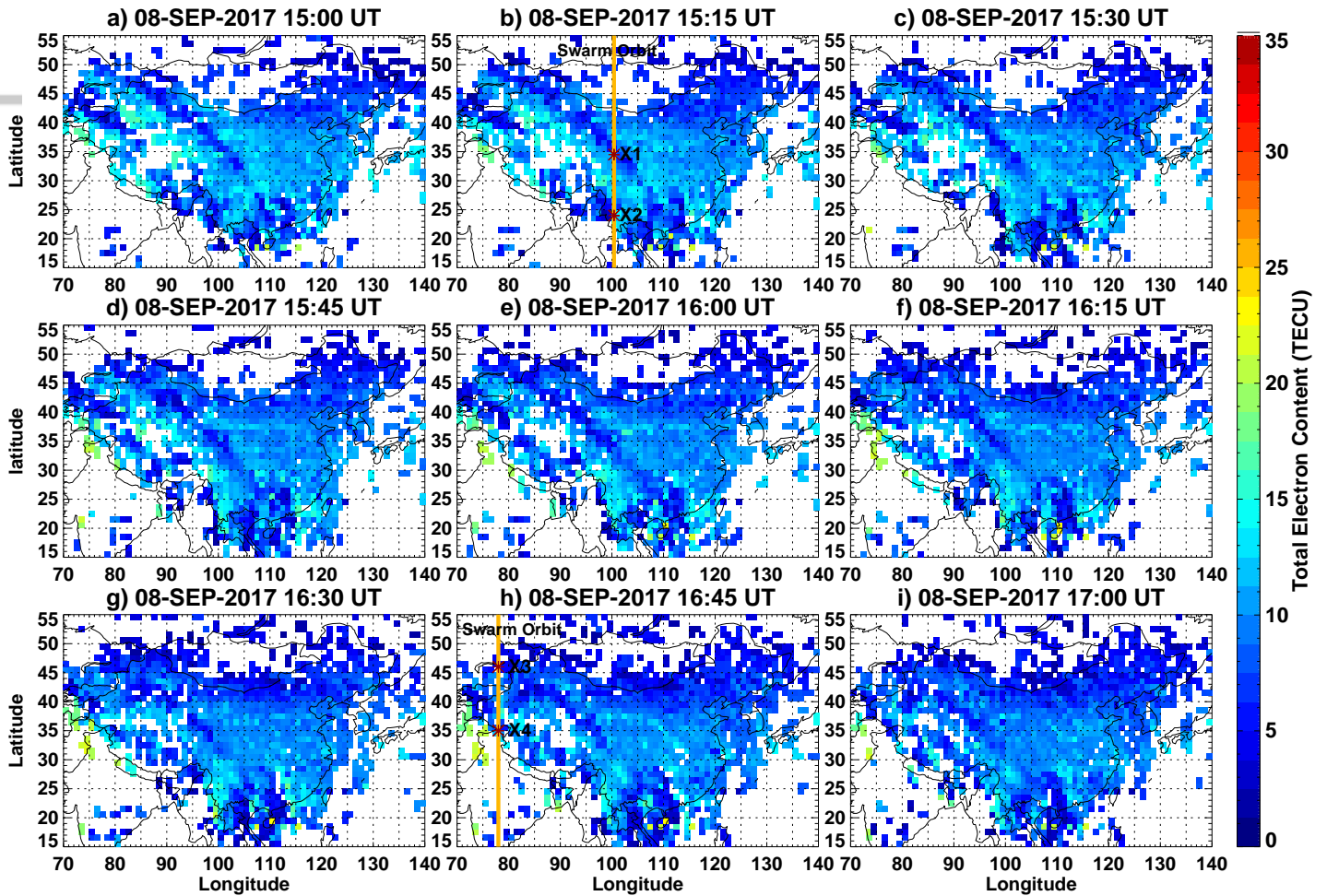


Figure 3. Same as Figure 2, but for time period of 15:00-17:00 UT on 08 September 2017. The Swarm satellite orbits are superimposed on TEC depletions for Figure 3b and 3h with four points of intersection being marked by asterisks.

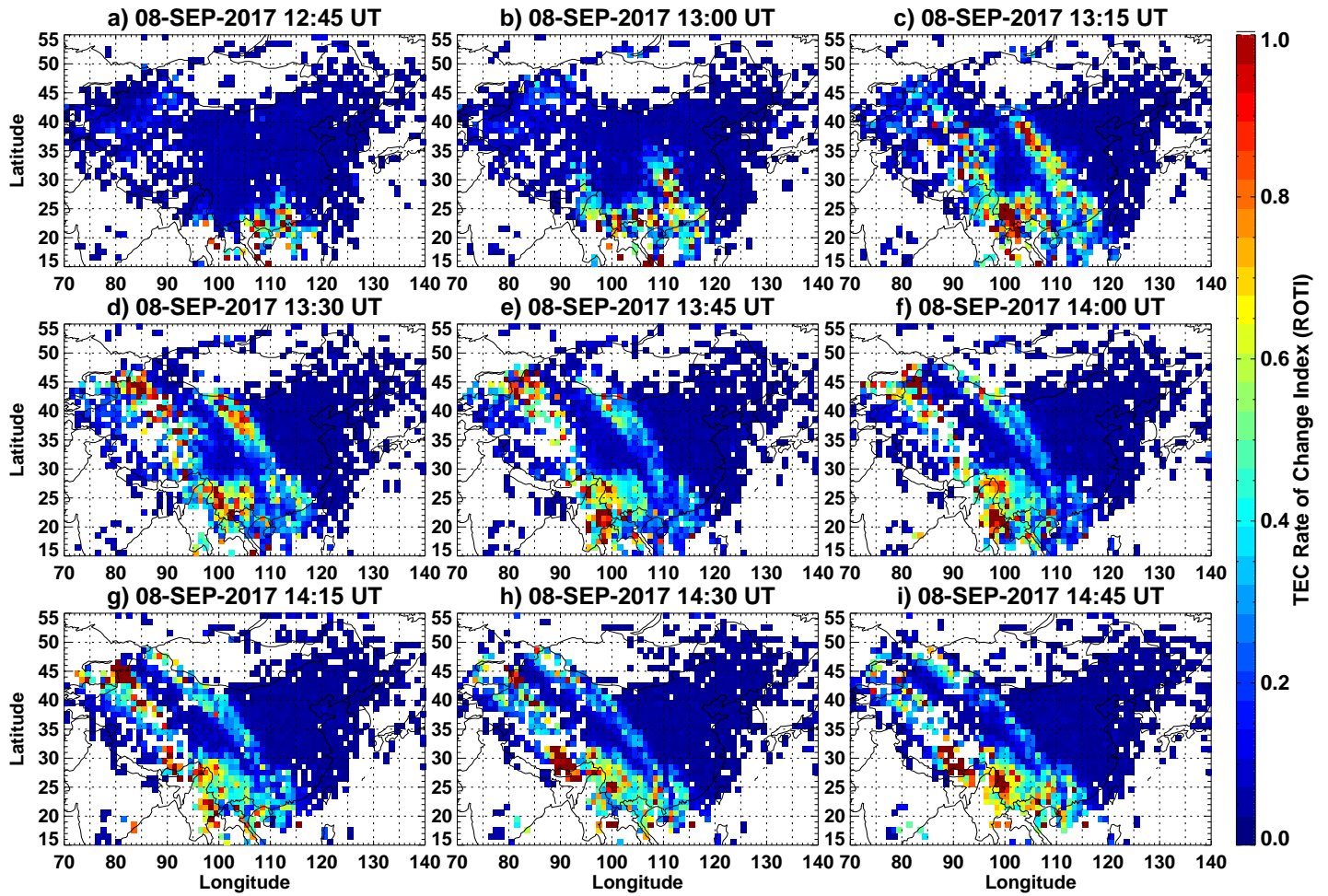


Figure 4. ROTI maps of ionospheric irregularities over China and adjacent areas with 15 min interval during 12:45-14:45 UT on 08 September 2017.

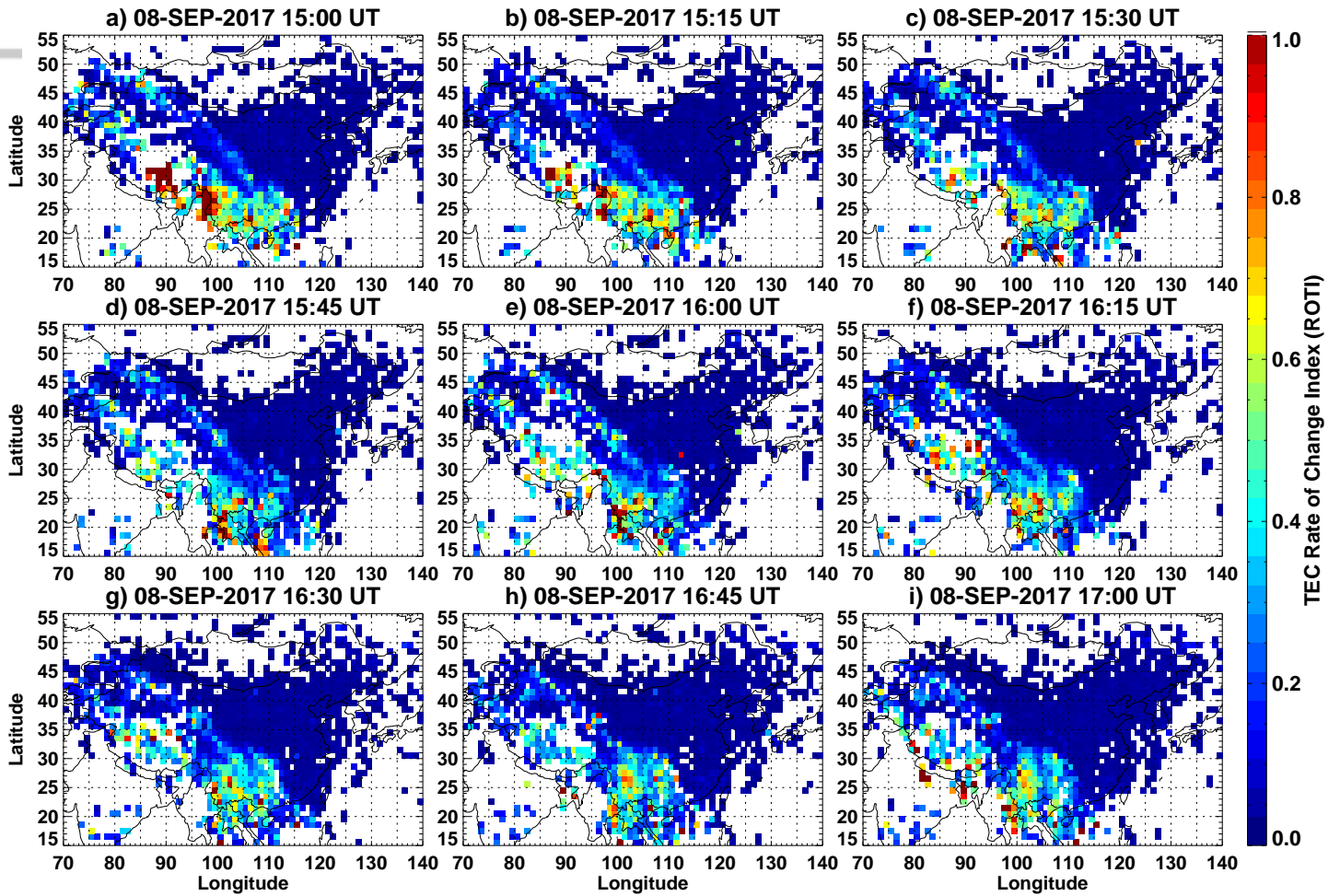


Figure 5. Same as Figure 4, but for time period of 15:00-17:00 UT on 08 September 2017.

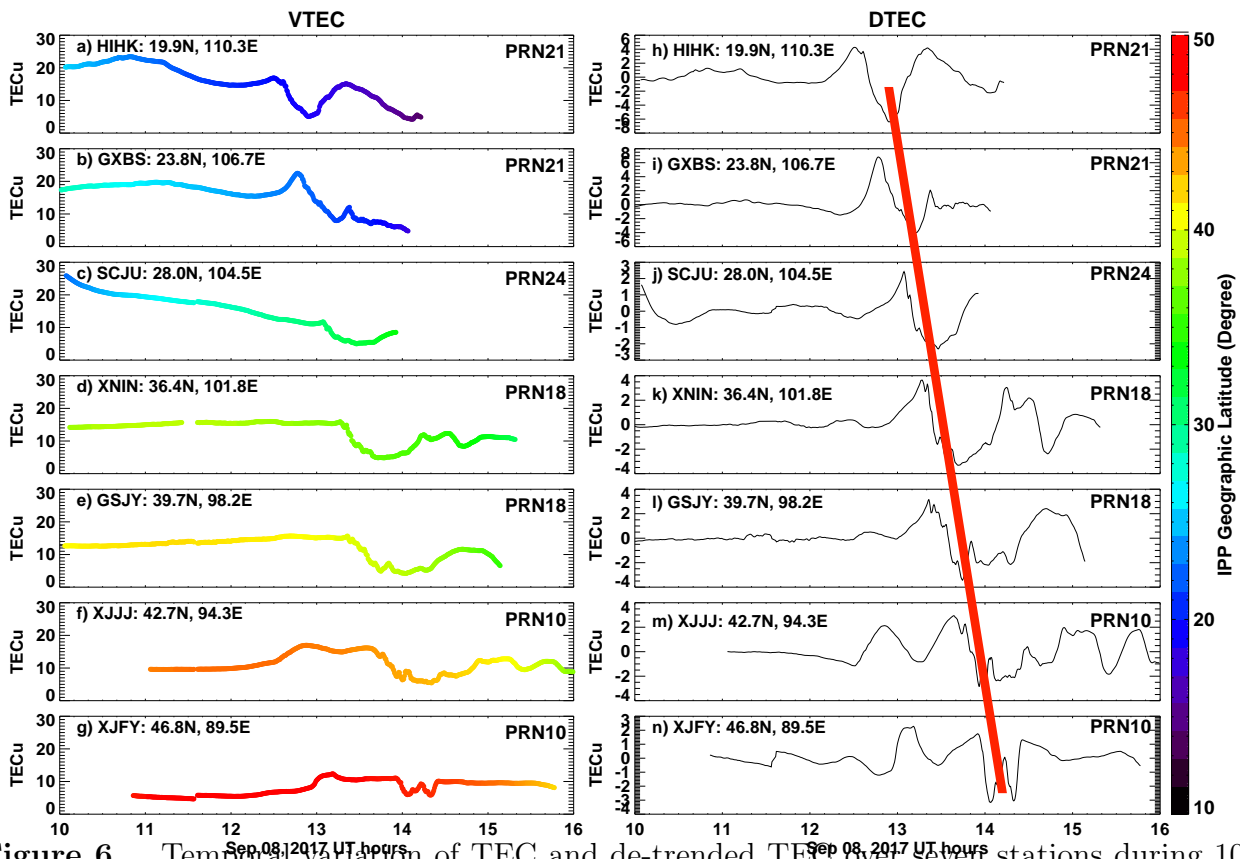


Figure 6. Temporal variation of TEC and de-trended TEC over seven stations during 10-16 UT on 08 September 2017. The color bar shows the geographic latitude range of the ionospheric pierce points (IPP). The red thick line marks the propagation of the depletions.

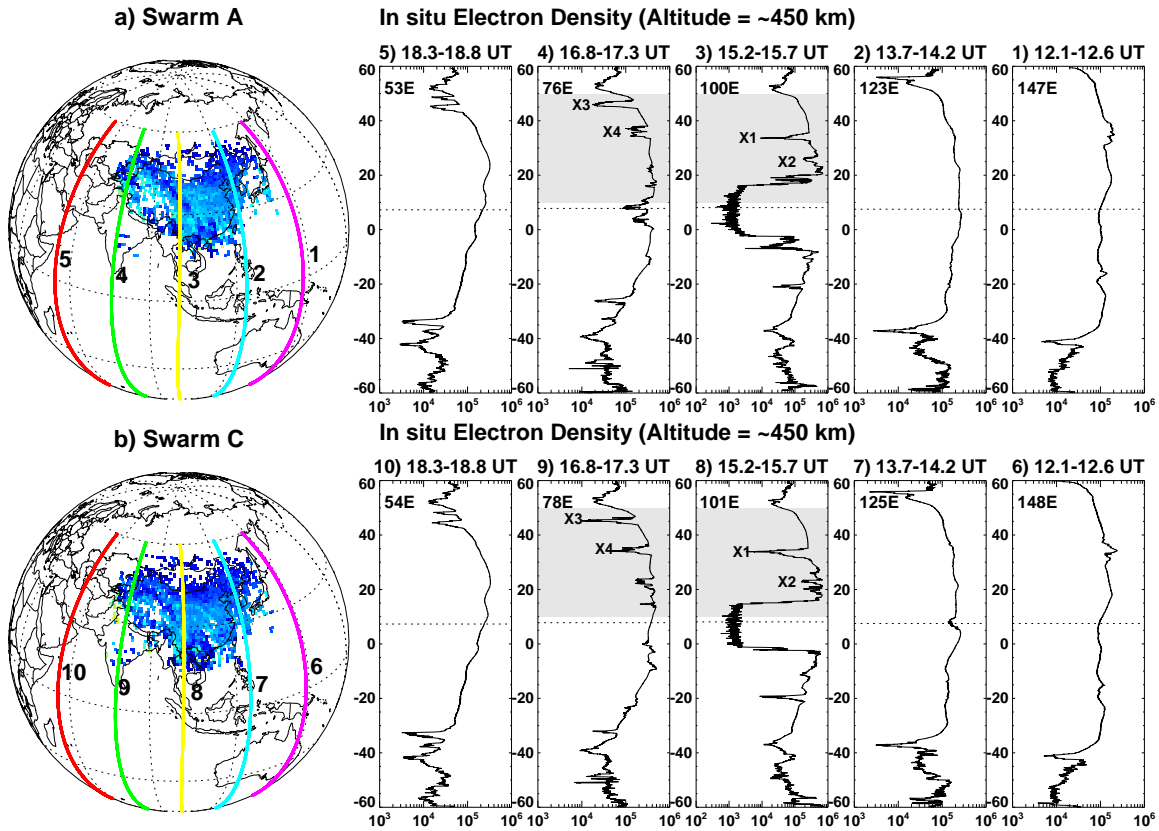


Figure 7. (a) (left) The global map with 5 different satellite orbit paths of Swarm A, with gridded TEC at 15:15 UT being superimposed; (right) variation of in situ electron density as a function of geographic latitudes along these paths. (b) the same as Figure 7a, but for Swarm C satellite with gridded TEC at 16:45 UT being superimposed. The shaded areas represent plasma depletions over China and adjacent regions. Four intersection points X1-X4 that marked in Figure 3b and 3h are also shown here. The magnetic equator is indicated by dotted horizontal lines on the density-latitude profiles.